Available online at www.sciencedirect.com
ScienceDirect
Trans. Nonferrous Met. Soc. China 32(2022) 3182−3196
Transactions of Nonferrous Metals Society of China
www.tnmsc.cn

Tailoring phase fractions of T' and η' phases in dual-phase strengthened Al−Zn−Mg−Cu alloy via ageing treatment

Yan ZOU[1], Xiao-dong WU[1], Song-bai TANG[1], Kai ZHAO[1], Ling-fei CAO[1,2]

1. International Joint Laboratory for Light Alloys (Ministry of Education), College of Materials Science and Engineering, Chongqing University, Chongqing 400044, China;
2. Shenyang National Laboratory for Materials Science, Chongqing University, Chongqing 400044, China

Received 25 August 2021; accepted 25 December 2021

Abstract: Hardness tests and transmission electron microscopy were used to investigate the strategy of tailoring the phase fraction of precipitates in an Al−Zn−Mg−Cu alloy strengthened by T' and η' phases. Different phase fractions of T' and η' phases are presented in samples subjected to either single or two stages of ageing treatments at 120 and 150 °C. For both types of ageing, the precipitation of η' phase is found to be promoted by ageing at lower temperature and its phase fraction increases with prolonging ageing time at 120 °C; whereas the phase fractions of T' and η' phases almost remain constant during ageing at 150 °C. Besides, the strain fields produced by T' and η' phases were analyzed by using the geometric phase analysis technique, and on a macroscale the contributions of T' and η' phases to precipitation strengthening have been quantitatively predicted by combining the size, phase fraction and number density of precipitates.

Key words: Al−Zn−Mg−Cu alloy; ageing behavior; microstructure; dual-phase strengthening

1 Introduction

Al−Zn−Mg−Cu alloys have been paid considerable attention in the past decades due to their high specific strength and wide applications [1,2]. As heat treatable alloys, the high strength of Al−Zn−Mg−Cu alloys attributes to the ageing precipitates formed during heat treatments. The fine precipitates at nanoscale can bring a great enhancement of strength due to their inhibition effect for the movement of dislocations [3−5]. The precipitation sequence is an important aspect in optimizing the heat treatment strategies, and it seems to be strongly dependent on alloy composition [6]. The η' phase, as a most common strengthening precipitate, has a hexagonal structure with a plate-like morphology [7,8]. Besides, the T' phase has also been reported to show strengthening effect [9,10], and it has a body-centred cubic structure with spherical morphology. In Al−Zn−Mg(−Cu) systems, their precipitation sequence has been reported as follows: supersaturated solid solution → Guinier−Preston (GP) zones → η' phase → η phase [9,11−13] or supersaturated solid solution →GP zones → T' phase → T phase [10,14]. The sequence is roughly classified by the Zn/Mg molar ratios of alloys, where the η' and η phases exist in alloys with Zn/Mg molar ratios over 2.2 and T' and T phases appear in alloys with Zn/Mg molar ratios below 2.2 [15].

The strength of Al−Zn−Mg−Cu alloys can be effectively enhanced by the increase of Zn content, causing a high Zn/Mg ratio. Thus, the η' phase and its precipitation behaviors have been focused in most of studies on Al−Zn−Mg−Cu alloys. Contrarily,

Corresponding author: Xiao-dong WU, Tel: +86-18581029651, E-mail: xiaodongwu@cqu.edu.cn;
Ling-fei CAO, Tel: +86-13996310689, E-mail: caolingfei@cqu.edu.cn
DOI: 10.1016/S1003-6326(22)66012-6

alloys strengthened by T' phase were paid much less attention due to the lack of excellent strengthening effect. However, a recent study has shown that the T' phase can contribute almost 200 MPa to the strength of Al−Mg alloys with the addition of Zn element [6,16], and these alloys also possess good toughness or formability. Additionally, it has been reported [17] that an Al−Zn−Mg alloy hardened by *T*-type phases shows good corrosion resistance, while keeping strength higher than that of 7150 alloy hardened by η' phase. A novel heat-resistant Al−Zn−Mg alloy [14] can be strengthened by numerous fine *T* phases, which distribute uniformly in the matrix and present a high yield strength of 200 MPa at 200 °C. The above research suggested that the formation of *T*-type phases contributes to the improvement of the corrosion resistance and thermostability of Al−Zn−Mg−Cu alloys.

The Al−Zn−Mg−Cu alloys have been widely applied in complex service environment, like elevated temperature [18] or acidic conditions [19], which would accelerate the failure and reduce the lifetime of materials. Therefore, it is imperative to develop alloys with excellent comprehensive performance, e.g., Al−Zn−Mg−Cu alloys with good corrosion resistance and thermostability. In previous studies, three-stage heat treatments, e.g. RRA [1,20] and the addition of trace elements, such as Er [21], Sc [22] and Ag [23] have been proposed to improve the corrosion resistance while keep desirable strength. However, these methods have not been extensively adopted in industrial production due to their complexity and costs. Therefore, more practical process is expected to ensure the comprehensive properties for Al−Zn−Mg−Cu alloys. For example, in the alloy strengthened by co-precipitation of T' phase and η' phase [24,25], tailoring the phase fraction of two phases with different properties can be effective.

Additionally, the strength is always of the greatest concern in Al−Zn−Mg−Cu alloys. At the nanoscale, the lattice strain introduced by precipitates is the key factor to influence its strengthening effect. Geometric phase analysis (GPA) technique has successfully been applied to the GP zones [26] and η' phase [27] in Al−Zn−Mg−Cu alloys. However, the strain field caused by the T' phase has not been investigated. Therefore, GPA was applied here to compare the strengthening effect of T' phase and η' phase.

To date, the ageing behavior and variation of phase fraction in dual-phase strengthened Al−Zn−Mg−Cu alloys have not been reported. Thus, in this study, ageing treatment was employed to tailor the phase fractions of T' phase and η' phase. The precipitates were characterized by using the transmission electron microscopy (TEM). Furthermore, the strain fields caused by T' phase and η' phase were compared to clarify the strengthening effect of precipitates at nanoscale, and the contribution of each precipitate to precipitation strengthening was also predicted at macroscale.

2 Experimental

A commonly used Al−Zn−Mg−Cu alloy was investigated in this study, with a nominal composition of Al−5.6Zn−2.5Mg−1.6Cu (wt.%) or Al−2.34Zn−2.81Mg−0.65Cu (at.%). The alloy was cast into an ingot with a thickness of 48 mm, and the ingot was homogenized at 460 °C for 6 h and 465 °C for 24 h with a heating rate of 30 °C/h, then air-cooled and hot-rolled (8 passes with a total reduction of 87.5%) at 460 °C to a 6 mm thin plate. All samples were cut from the plate and then solution-treated at 470 °C for 1 h followed by water quench to room temperature. Subsequently, the samples were artificially aged to peak ageing condition through four different paths in an oil bath, which are illustrated in Fig. 1. The samples aged at a low temperature of 120 °C followed by a high temperature ageing at 150 °C were named as LH samples; similarly, samples aged at 150 °C followed by ageing at 120 °C were named as HL samples.

Hardness measurements were performed on a Vickers hardness tester with an 1 kg load and a dwelling time of 15 s, and at least five individual measurements were recorded to calculate the average value. The foil samples for transmission electron microscopy (TEM) were prepared by mechanically polishing to 70 μm and then by double-jet electropolishing in a solution of 25% nitric acid and 75% methanol at the temperature below −25 °C. TEM observations were performed on an FEI Tecnai G^2 F20 microscope operated at 200 kV. The size of precipitates was measured by using a Nano Measure 1.2 software based on the

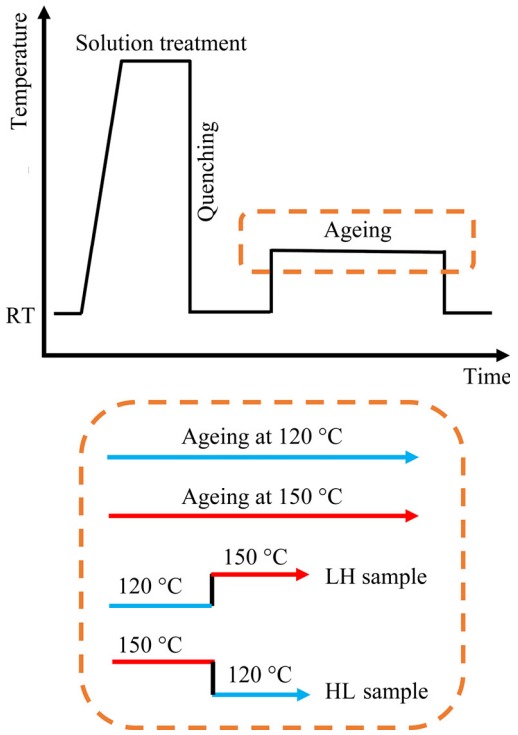

Fig. 1 Schematic illustration of sample treated by different ageing paths

bright field TEM images, and at least five images from different zones were taken into account for each condition. The GP zones were negligible in investigated ageing conditions. Thus, only T' and η' phases were considered in this work. The phase fraction was defined as the ratio of the count of T'/η' phase to the total count of precipitates, and each phase was evaluated by counting the number of precipitates with different morphologies from the TEM images along $[110]_{Al}$ and $[112]_{Al}$ zone axes, and the method was described in detail in our previous work [28]. GPA was adopted to calculate the strain field caused by ageing precipitates, for which the plugin script was installed in Gatan DigitalMicrograph software and the high resolution TEM (HRTEM) images used for GPA were processed by the HRTEM filter plugin script to remove the background noise [29].

3 Results

3.1 Single-stage ageing

Figure 2 shows the hardening curves of samples respectively aged at 120 and 150 °C for various time. The hardness value increases rapidly from HV 78.5 to HV 172.3 during ageing at 120 °C for 24 h; whereas, it displays a lower peak hardness of HV 153.5 and the time to peak decreases to 16 h when the sample is aged at 150 °C. The elevated ageing temperature can largely accelerate the ageing process with a certain loss of peak hardness.

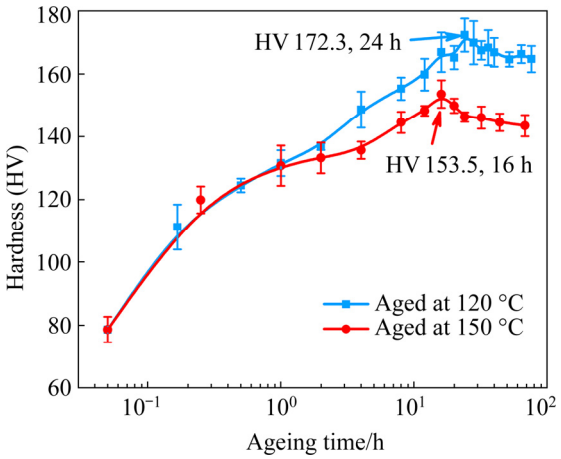

Fig. 2 Hardening curves of samples aged at 120 and 150 °C

The bright field TEM images of samples at different ageing stages are displayed in Fig. 3. When aged at 120 °C for 0.5 h, the sample obtains numerous precipitates uniformly distributed in the matrix, among which few large plate-like and dense spherical precipitates can be observed in Fig. 3(a), and the corresponding selected area electron diffraction pattern (SADP) shows no diffraction spots of precipitates due to their extremely fine size. Thus, these precipitates are further characterized by HRTEM. Figure 4(a) shows the HRTEM image of precipitates with round projections (as indicated by red arrows), and they are identified as GP I zone as indicated by the fast Fourier transform (FFT) diffractogram (Fig. 4(b)) [30]. The HRTEM image of plate-like phase in Fig. 3(a) is shown in Fig. 4(c), which is proved as η' phase by the FFT diffractogram (Fig. 4(d)) [31]. Thus, the GP I zone is the main precipitate in sample aged at 120 °C for 0.5 h. After ageing for 12 h (Fig. 3(b)), precipitates grow bigger and show round and plate-like projections. Inserted SADP shows diffraction spots at 2/5 and 3/5 $[220]_{Al}$, which are indexed as T' phase with round projections. And the plate-like phases are η' phases as mentioned above. Under peak-aged condition (24 h), the mean diameter of precipitates (Figs. 5(a_1) and (a_2)) increases to (3.1±0.6) nm for T' phase and (4.3±0.9) nm for η' phase, respectively. However, the ageing process is

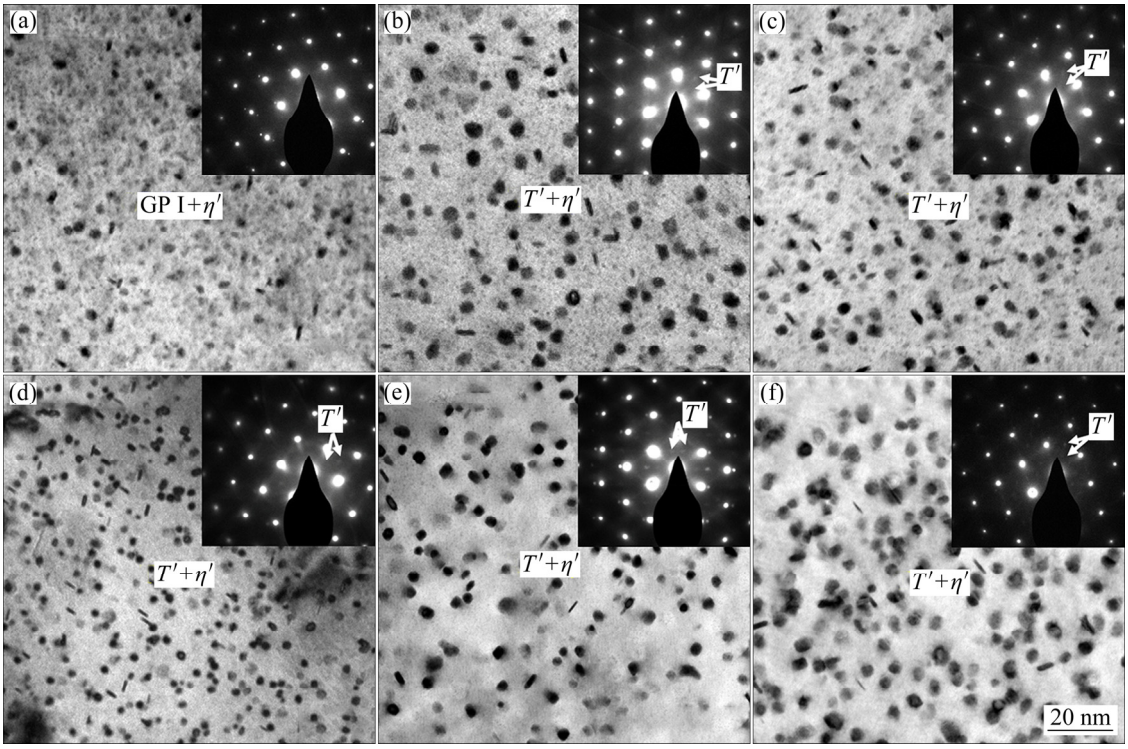

Fig. 3 TEM images taken from samples aged at 120 °C for 0.5 h (a), 12 h (b) and 24 h (c); 150 °C for 0.5 h (d), 8 h (e) and 16 h (f) along $[110]_{Al}$ zone axis

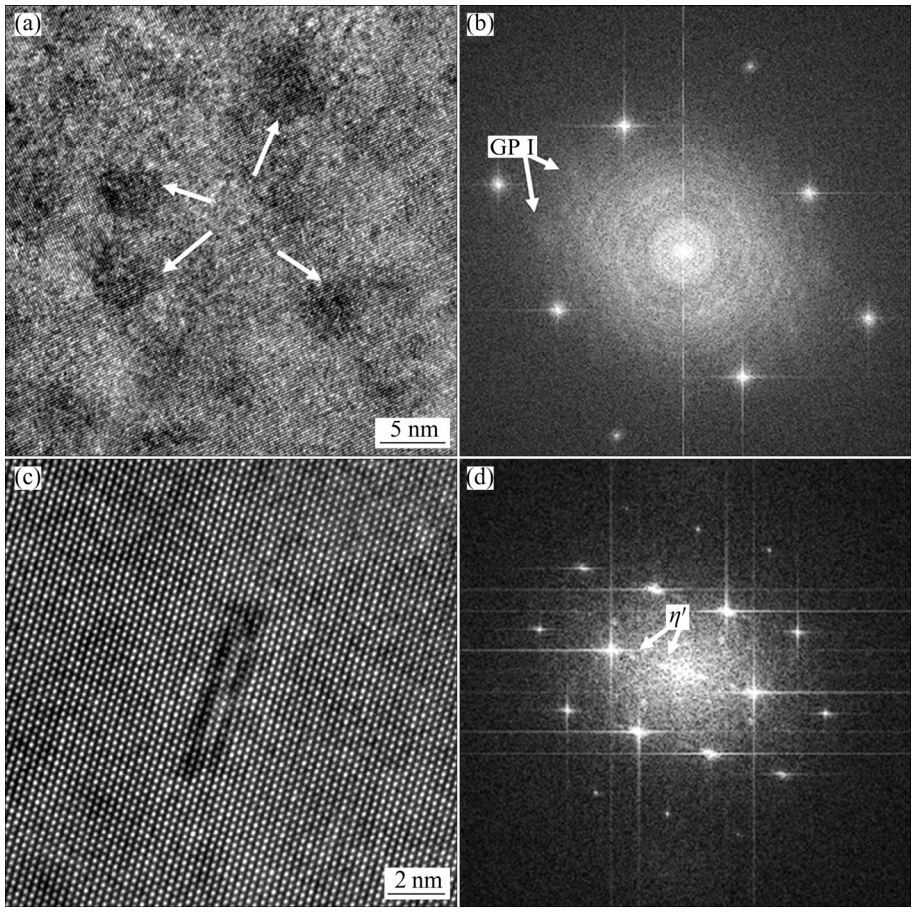

Fig. 4 HRTEM images (a, c) and corresponding FFT diffractograms (b, d) of precipitates in samples aged at 120 °C for 0.5 h: (a, b) GP I; (c, d) η' phase

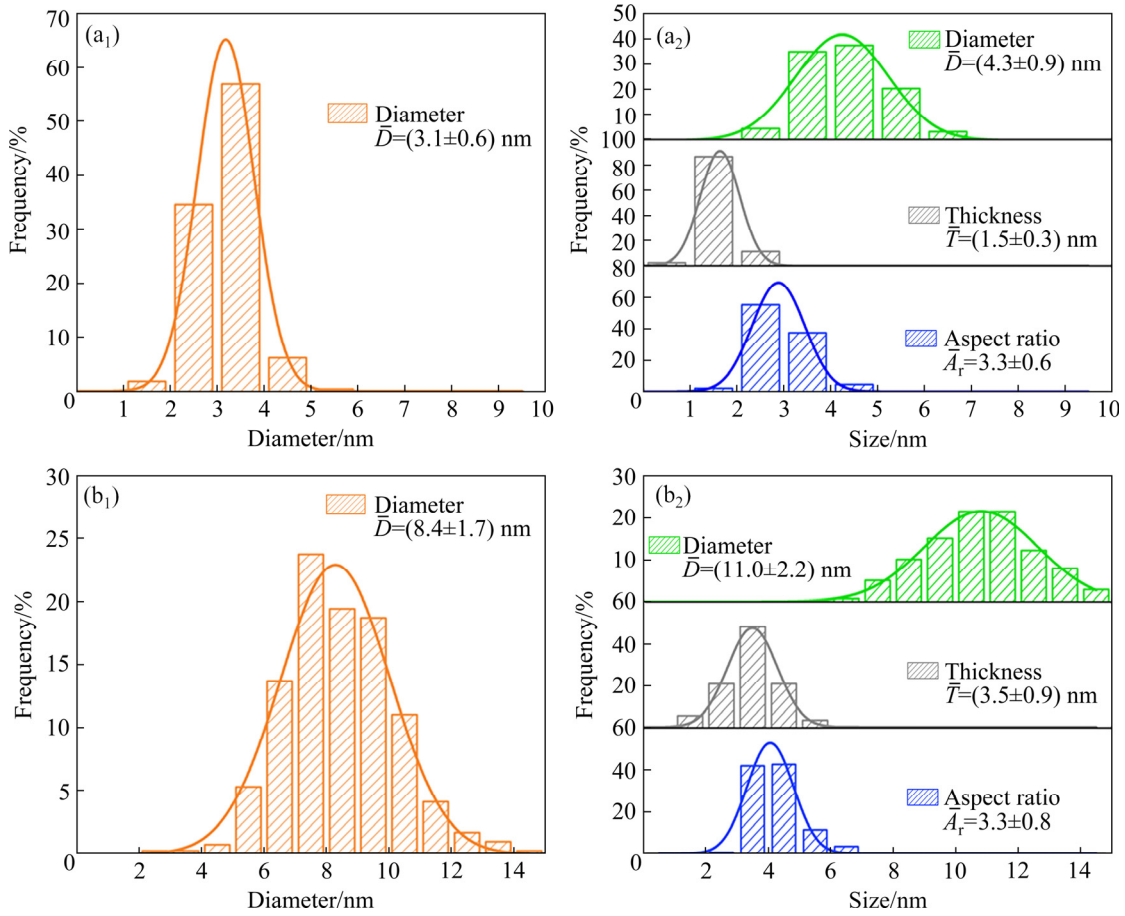

Fig. 5 Size distribution of T' (a_1, b_1) and η' (a_2, b_2) phases peak-aged at 120 °C for 24 h (a_1, a_2) and 150 °C for 16 h (b_1, b_2)

accelerated by elevating the ageing temperature to 150 °C, where T' phase and η' phase dominate at the early stage of ageing for 0.5 h (Fig. 3(d)) and their sizes are larger than those in Fig. 3(a) aged at 120 °C for the same period. With increasing ageing time at 150 °C (Figs. 3(e) and (f)), T' phase and η' phase are still the main precipitates, and their sizes are visibly larger than those aged at 120 °C. Compared with the size distribution in Figs. 5(a_2) and (b_2), it can be seen that η' phases obtain different sizes after ageing at different temperatures, but their mean aspect ratio (the ratio of diameter to thickness) is a constant of 3.3.

Growth kinetics of the T' phase and η' phase during single stage ageing at different temperatures is shown in Fig. 6(a). The growth rate of the radius (r_p) is well fitted by the power-law equation [32]:

$$r_p = kt^{1/2} \quad (1)$$

where t is the ageing time, and k is a function of the supersaturation, diffusion coefficient, and aspect ratio of precipitates. As a parameter, k is simply to characterize the growth rate of the T' phase and η' phase. Comparisons among the value of k explain that the growth kinetics is accelerated when ageing temperature increases, i.e., both precipitates are more easily coarsened at 150 °C due to higher growth rate. Both T' phase and η' phase show the same growth rate of 0.14 nm/h$^{1/2}$ at 120 °C, while η' phase exhibits a faster growth rate of 0.54 nm/h$^{1/2}$ than that of T' phase (0.39 nm/h$^{1/2}$) at 150 °C. Figures 6(b) and (c) show the variation of the relative phase fractions of the T' phase and η' phase during the ageing process. After ageing at 120 °C for 0.5 h, few T' and η' phases form with the dominance of GP zones. With the ageing time increasing to 12 h, the phase fraction of η' phase reaches 25% and it increases to 46% after ageing for 24 h; meanwhile, the phase fraction of T' phase decreases with the increase of ageing time. Unlike ageing at 120 °C, the phase fractions of the T' phase and η' phase are almost unchanged during ageing at 150 °C. Such interesting phase evolution brings great potential to tailoring the phase fractions of T'

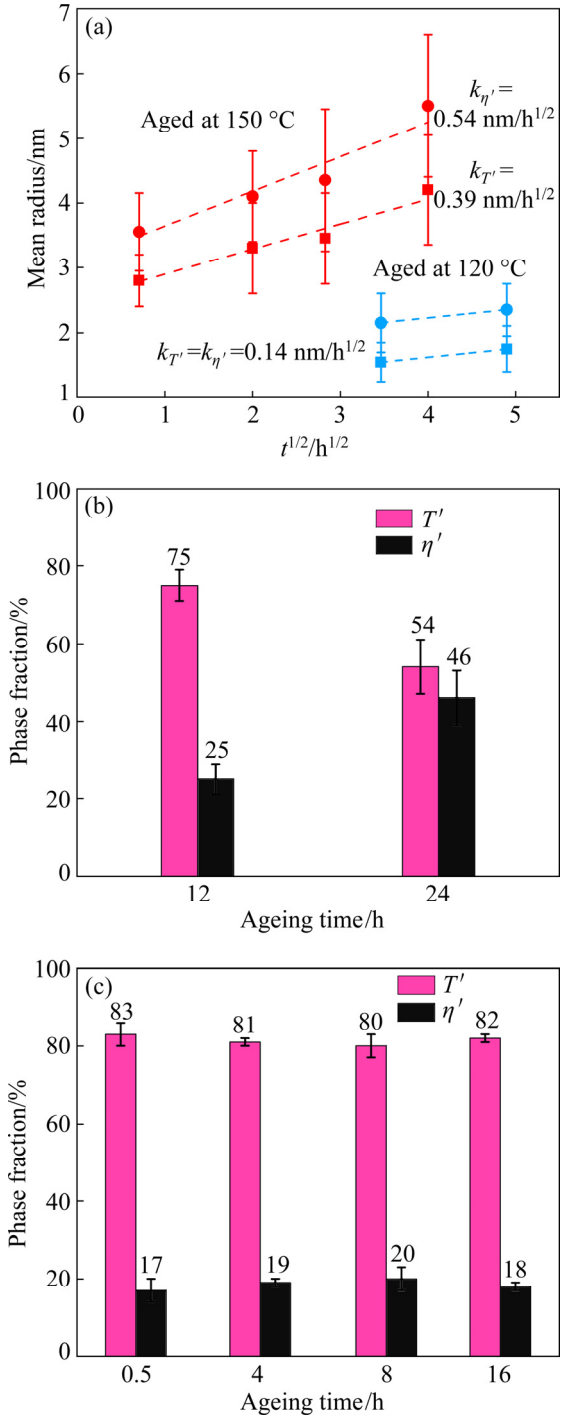

Fig. 6 Growth kinetics and results on evolution of precipitate radius with $t^{1/2}$ during single- stage ageing (a), and phase fractions of T' and η' phases during ageing at 120 °C (b) and 150 °C (c)

phase and η' phase by adjusting different ageing treatments, so as to change the comprehensive properties of the alloy.

3.2 Two-stage ageing

In order to verify the regulation of phase fraction, a series of two-stage ageing treatments were designed, as shown in Fig. 1. A shorter time (0.5 h) and longer time of 8 h and 12 h (half of the peak-aged time when single-stage is aged at 120 °C or 150 °C, i.e., 24 h at 120 °C and 16 h at 150 °C) were adopted in the first stage of ageing, and then samples were aged to peak ageing condition at 120 or 150 °C. The hardness value corresponding to each ageing treatment is listed in Table 1. It is clear that samples after two-stage ageing treatments show similar hardness as compared to single-stage ageing (LH samples versus samples aged at 120 °C, and HL samples versus samples aged at 150 °C), while the phase fraction of precipitates has changed.

Table 1 Hardnesses of samples under different ageing treatments

Sample	Ageing treatment	Hardness (HV)
$L_{0.5}H_{12}$	(120 °C, 0.5 h) + (150 °C, 12 h)	170.1±4.3
$L_{12}H_2$	(120 °C, 12 h) + (150 °C, 2 h)	171.4±2.4
$H_{0.5}L_8$	(150 °C, 0.5 h) + (120 °C, 8 h)	152.5±4.3
H_8L_{20}	(150 °C, 8 h) + (120 °C, 20 h)	162.7±5.0

L_xH_y means (120 °C, x h) + (150 °C, y h), and H_xL_y means (150 °C, x h) + (120 °C, y h)

In order to further clarify the relationship among ageing parameters, hardness and microstructure, TEM images obtained from samples listed in Table 1 are shown in Fig. 7 and the size distribution of precipitates is shown in Fig. 8. In the peak-aged condition, the main precipitates are still T' phase and η' phase in all LH and HL samples, which are of the same type of precipitates in the single-stage ageing at 120 and 150 °C. For the $L_{0.5}H_{12}$ sample, dense distribution of precipitates can be observed (Fig. 7(a)), which consists of 78% spherical T' phase with 22% plate-like η' phase, and their size distribution is shown in Figs. 8(a_1) and (a_2). In this case, the mean diameters of the T' phase and η' phase are (5.2±1.1) nm and (5.8±1.4) nm, respectively. After a relatively long time (12 h) of ageing at 120 °C as the first step, the time to peak in the second-stage ageing at 150 °C significantly decreases from 12 to 2 h, resulting in a higher number density of fine precipitates in the $L_{12}H_2$ sample, as shown in Fig. 7(b) and Figs. 8(b_1) and (b_2). Besides, the aspect ratios of η' phase achieve the same value of 2.6 in the $L_{0.5}H_{12}$ and $L_{12}H_2$

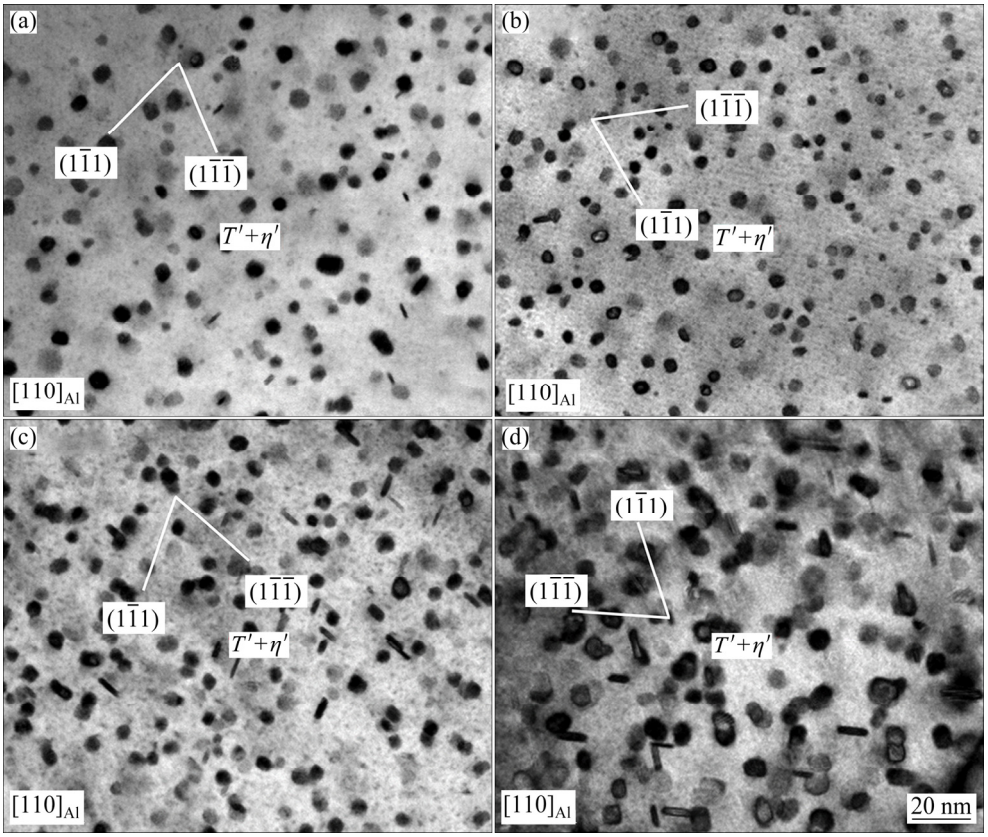

Fig. 7 TEM images of samples along $[110]_{Al}$ zone axis under different ageing treatments: (a) $L_{0.5}H_{12}$; (b) $L_{12}H_2$; (c) $H_{0.5}L_8$; (d) H_8L_{20}

samples. For the $H_{0.5}L_8$ sample, the precipitates are slightly bigger than those in LH samples. The mean diameter (Figs. 8(c_1) and (c_2)) reaches (6.0±1.0) nm for T' phase and (7.3±1.2) nm for η' phase, and the aspect ratio of η' phase increases to 3.7. Contrary to LH samples, for HL samples, the time to peak ageing in the second-stage increases with the extension of first-stage ageing, e.g., if the first-stage ageing time prolongs from 0.5 to 8 h, the time to peak in the second-stage ageing increases from 8 to 20 h. Consequently, the coarsening of precipitates is evident in the H_8L_{20} sample due to a long time of first-stage ageing at 150 °C. The average diameters of T' phase and η' phase in H_8L_{20} sample are (6.7±1.3) nm (Fig. 8(d_1)) and (9.8±2.6) nm (Fig. 8(d_2)), which are about 12% and 34% greater than those in $H_{0.5}L_8$ sample, respectively.

The growth kinetics of the T' phase and η' phase during the second-stage ageing is shown in Fig. 9(a). For HL samples, the coarsening of precipitates mainly occurs during the first-stage ageing at 150 °C, and the variation of precipitate size is negligible during the second-stage ageing at 120 °C due to the tiny value of k (smaller than 0.1 nm/h$^{1/2}$). However, for LH samples, although a high growth rate (1.44−1.62 nm/h$^{1/2}$) of precipitate is evident during the second-stage ageing at 150 °C, their precipitates remain smaller sizes than those in HL samples due to a short dwelling time at 150 °C (2 h for $L_{12}H_2$ sample, 8 and 20 h for HL samples).

The phase fractions of T' phase and η' phase during the ageing process are compared in Fig. 9(b). It is clear that the phase fraction in LH samples is much different from that in the HL samples caused by the difference in ageing routes. The precipitates in the $L_{12}H_2$ sample consist of 74% T' phase and 26% η' phase, which is very close to that in the L_{12} sample (aged for 12 h at 120 °C). This means that the phase fractions of the T' phase and η' phase are almost unchanged during the second-stage ageing at 150 °C. Meanwhile, as listed in Table 1, the peak hardnesses of the $L_{0.5}H_{12}$ and $L_{12}H_2$ samples are HV 170.1 and HV 171.4, respectively, which are similar to those of sample aged at 120 °C for 24 h, but with an improved phase fraction of T' phase from 54% to 74%−78%. In the HL samples, however, the improved phase fraction of η' phase is visible during the second-stage ageing at 120 °C, as

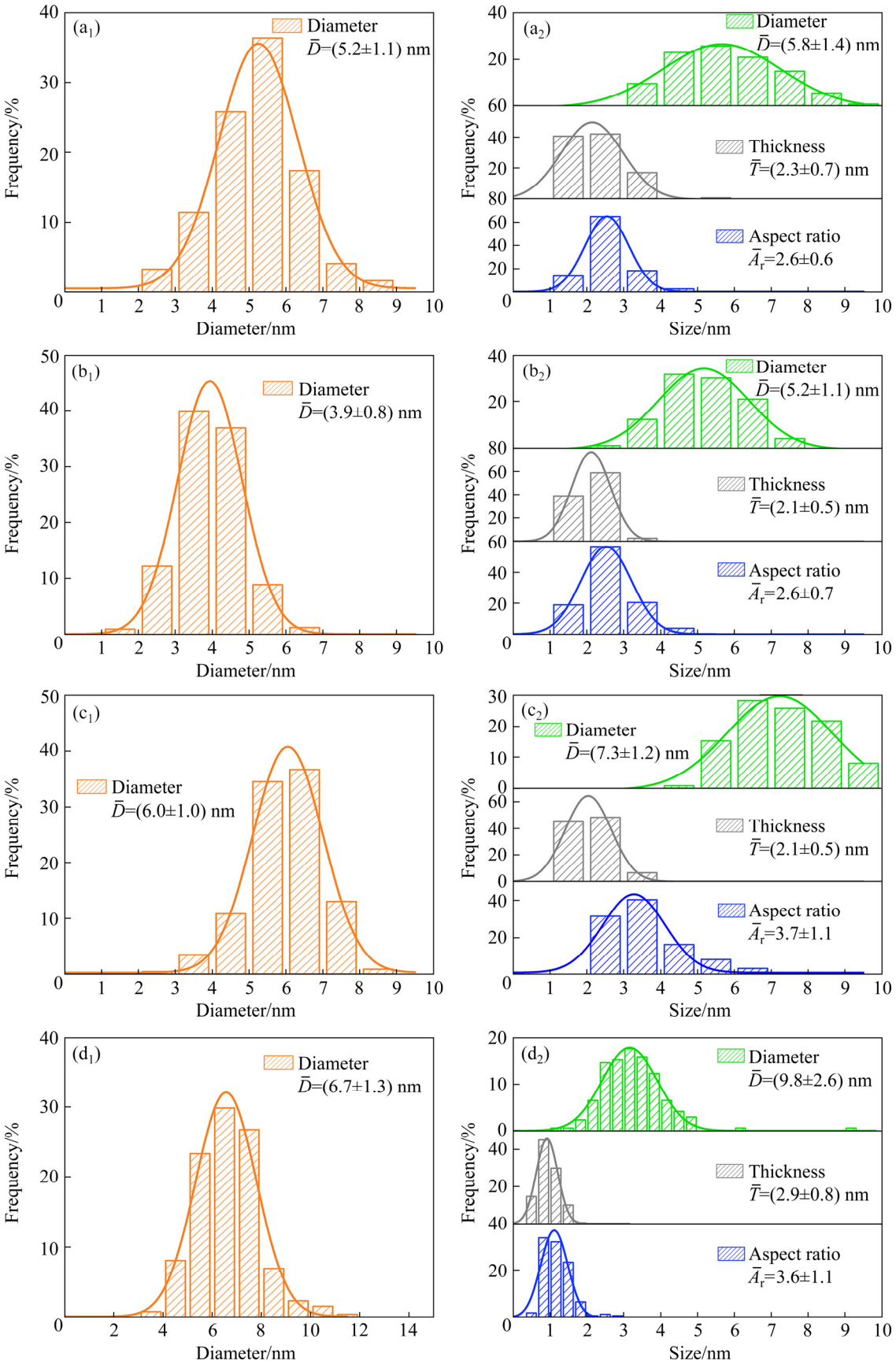

Fig. 8 Size distribution of T' (a_1, b_1, c_1, d_1) and η' (a_2, b_2, c_2, d_2) phases in samples after different ageing treatments: (a_1, a_2) $L_{0.5}H_{12}$; (b_1, b_2) $L_{12}H_2$; (c_1, c_2) $H_{0.5}L_8$; (d_1, d_2) H_8L_{20}

shown in Fig. 9(b), which increases from 17% to 33% and 20% to 28% in the $H_{0.5}L_8$ and H_8L_{20} samples, respectively. Besides, the peak hardness of $H_{0.5}L_8$ sample is HV 152.5, which is lower than HV 162.7 of the H_8L_{20} sample.

In order to compare the strengthening effect of T' phase and η' phase, their strain fields are quantitatively measured by employing GPA technique. The distribution of the strains for representative T' phase and η' phase is demonstrated in Fig. 10. As shown in Fig. 10(a), the edge-on configuration of η' phase is presented and the interface between precipitates and the matrix is manually distinguished by the yellow dash curve. At the same time, the x-axis is set to be parallel to $[1\,\bar{1}\,1]_{Al}$ direction and the y-axis is set to be vertical to $[1\,\bar{1}\,1]_{Al}$ direction. Figures 10(b) and (c) show the strain maps of ε_{xx} and ε_{yy}, and the color scale represents a range of strain from −10% to 10%. Obvious strain field is visible at the interface of η' phase and the matrix along the $(1\,\bar{1}\,1)_{Al}$ plane. The upper interface is positive ε_{xx} strain, while the bottom interface is negative ε_{xx} strain, indicating the uneven distortion of interplanar spacings of $(1\,\bar{1}\,1)_{Al}$. The maximum ε_{xx} strain is measured to be 2.4%. In contrast, strain in the ε_{yy} strain map is tiny and uniform, and the maximum εyy strain is measured to be 1.1%, which is much smaller than

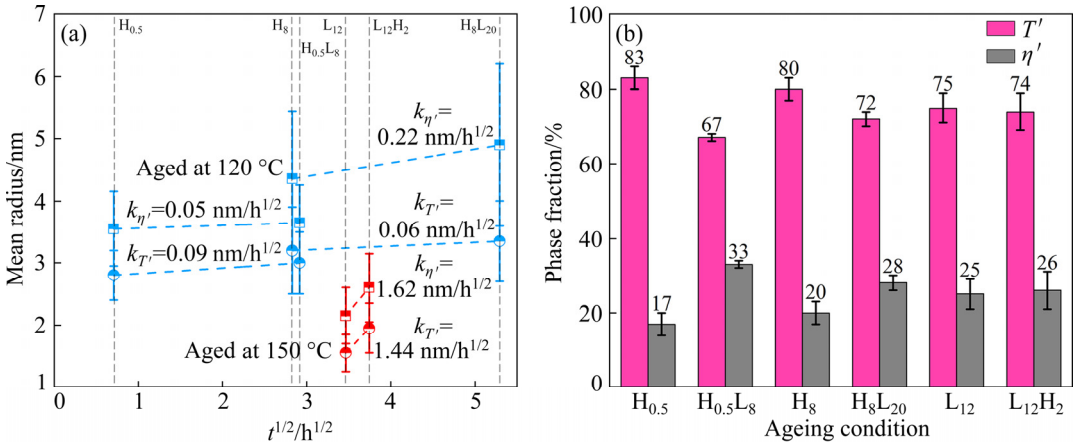

Fig. 9 Growth kinetics and results on evolution of precipitate radius with $t^{1/2}$ (a) and phase fractions of T' and η' phases during second-stage ageing (b)

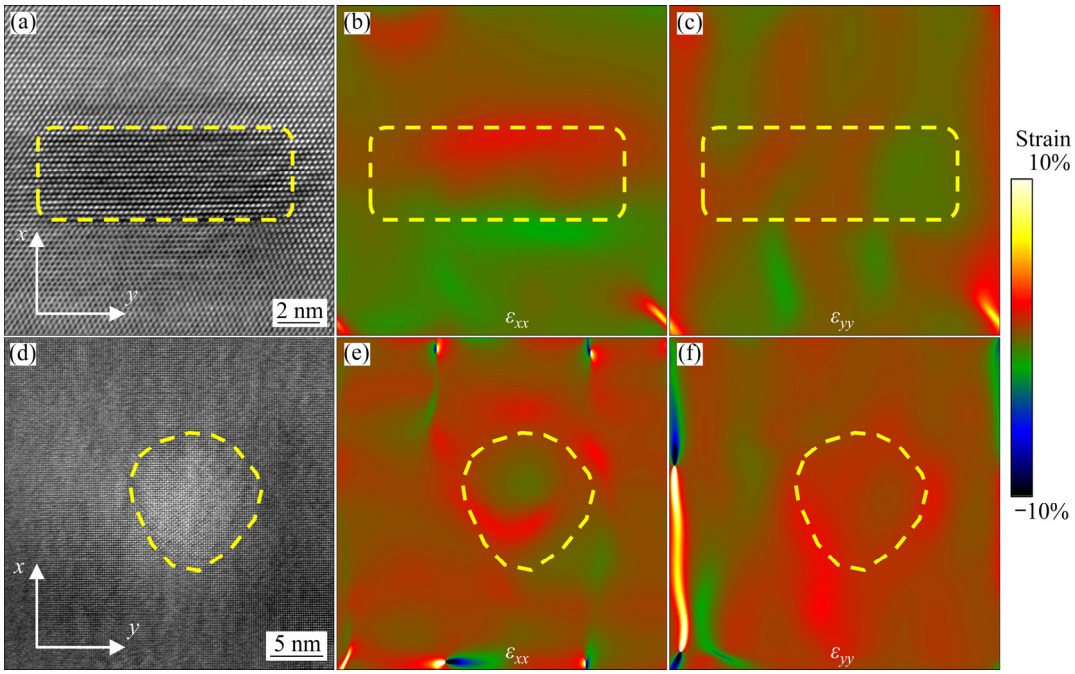

Fig. 10 Representative HRTEM images of η' (a) and T' (d) phases, and corresponding strain maps along x (b, e) and y (c, f) directions

ε_{xx} strain. The measured strain in the present work is matched well with the simulated results for η' phase, in which ε_{xx} strain is 2.2% and ε_{yy} strain is 1.2% [27]. Figure 10(d) shows the spherical morphology of the T' phase, the x-axis is set to be parallel to $[010]_{Al}$ direction and the y-axis is set to be parallel to $[100]_{Al}$ direction. The strain maps of the T' phase are presented in Figs. 10(e) and (f), where the strain mainly distributes along the interface of the T' phase and the matrix. Besides, the difference between ε_{xx} and ε_{yy} strains is smaller than that of η' phase, for which the maximum ε_{xx} and ε_{yy} strains are approximately 1.2% and 1.5%, respectively. It may be caused by the spherical morphology of the T' phase.

4 Discussion

4.1 Ageing behavior during single-stage ageing

Figure 3 shows the representative TEM micrographs of the alloys during ageing at 120 and 150 °C, which mainly contain the T' phase and η' phase. When the samples are aged at 120 °C, numerous GP zones have been formed after 0.5 h (Fig. 3(a)), and their number density of precipitates is higher than that of samples aged at 150 °C (Fig. 3(d)). This correlates well with the conclusion that the formation of GP zones is more beneficial at lower ageing temperatures [9,33]. The size evolution of T' phase and η' phase is summarized in Fig. 6(a) as a function of ageing time. The precipitates show a higher growth rate in size at the high ageing temperature of 150 °C than at 120 °C, which is caused by the higher diffusion rates of solutes. The diffusion coefficient of solutes (D_1) in the Al−Zn−Mg−Cu alloys at a certain temperature can be calculated by the Arrhenius equation [34]:

$$D_1=D_0\exp[-Q/(RT)] \quad (2)$$

where D_0 is the pre-exponential factor, Q is the activation energy, R is the molar gas constant and T is the thermodynamic temperature. It can be seen that the diffusion coefficient D_1 increases with the increase of ageing temperature. The diffusion coefficients of Zn ($D_{1,Zn}$) and Mg ($D_{1,Mg}$) at 150 °C are 13.4 times and 12.1 times of those at 120 °C [34], respectively, which causes T' phase and η' phase to grow larger with a faster growth rate in radius at higher ageing temperature. Besides, as to the lower ageing temperature of 120 °C, the reduced size discrepancy of precipitates (Figs. 5(a_1) and (a_2)) relieves the chemical potential between precipitates, which resultantly decreases the driving forces of Ostwald ripening [34]. In sample peak-aged at 150 °C with large size disparity (Figs. 5(b_1) and (b_2)), the small precipitates can dissolve rapidly to feed the large ones to grow, leading to the reduction of number density for precipitates (Fig. 3(f)).

It is noteworthy that the variation of phase fractions of T' phase and η' phase increases with the increase of ageing time at 120 °C while it remains constant when the sample is aged at 150 °C (Figs. 6(b) and (c)). This indicates that the precipitation of T' phase and η' phase is sensitive to the ageing temperature. A similar variation of the T' phase has also been reported in Al−Mg−Zn−Cu alloy with increasing ageing temperatures [34]. Generally, the nucleation and growth of precipitates occur during the ageing process, in which the nucleation is determined by a preferential clustering and the growth is controlled by diffusion and attachment of solutes [16]. In Al−Zn−Mg−Cu alloys, the vacancies introduced by quenching play an important role in the formation of GP zones. Vacancy-rich GP zones and solutes-rich GP zones are considered to possess different transition pathways, where the former can be transformed into T' phase and the latter can be transformed into η' phase [10,35]. In the present study, vacancies can be trapped by Mg atoms easily due to their stronger vacancy bonding energy than Zn or Cu atoms [35,36]. A proportion of these Mg−vacancies complexes (vacancy-rich GP zones) transformed into T' phase directly. Besides, the diffusion coefficients of Zn and Mg are 3.11×10^{-21} and 3.24×10^{-21} m^2/s, respectively, far way greater than that of Cu (8.40×10^{-23} m^2/s) [34]. Thus, the other proportion of Mg−vacancies complexes preferentially cluster with Zn atoms due to their opposite size effect of Zn and Mg atoms (atom radius: $r_{Mg}>r_{Al}>r_{Zn}$) in the Al matrix, which relieves the strain energy of the matrix, leading to the formation of Mg−Zn−vacancies complexes. And the Mg−Zn−vacancies (solutes-rich GP zones) gradually transform into η' phases during the subsequent ageing process at 120 °C, which explains the increase of the phase fraction of η' phase, as shown in Fig. 6(b). Due to excessive content of Mg relative to that of Zn (Zn/Mg molar

ratio=0.83) in the investigated alloy, most GP zones are Mg-rich with a Zn/Mg molar ratio lower than 1, which tend to transform into T' phase [28], leading to the domination of T' phase at 120 °C.

When the ageing temperature increases to 150 °C, the diffusion of Cu atoms is remarkably facilitated and its diffusion coefficient increases to 1.53×10^{-21} m^2/s, which is closer to the diffusion coefficients of Zn (3.93×10^{-20} m^2/s) and Mg (4.17×10^{-20} m^2/s) atoms than the case at 120 °C [34]. Meanwhile, Cu atoms and Zn atoms are 14.6% and 1.9% smaller than Al atoms [37], which increases the possibility of Mg−vacancies complexes bonding to Cu atoms to relax the strain in the matrix. Thus, the Cu concentration in solutes-rich GP zones increases with a parallel decrease in the Zn concentrations, leading to the decrease of Zn/Mg molar ratio for GP zones, which promotes the transformation from GP zones to T' phases. Thus, the proportion of the T' phase is much higher than that of the η' phase when the sample is aged at 150 °C. Furthermore, the phase fractions of T' phase and η' phase are almost invariable during ageing at 150 °C, which suggests that the formation of most T' phase and η' phase has completed at the early stage of ageing (less than 0.5 h) due to fast diffusion of solutes [28], and the transformation from GP zones to T' phases and η' phases reaches a dynamic balance during the subsequent ageing process.

4.2 Ageing behavior during two-stage ageing

Two types of combination of ageing have been designed in this work: one follows the ageing path of low temperature + high temperature (LH), and the other is converse (HL). As for LH samples, we have applied a first ageing at 120 °C followed by the second one at 150 °C. Prolonging ageing time at the first stage can reduce the time to reach the peak hardness at the second stage, as listed in Table 1. This is caused by the growth of precipitates at the first stage of ageing, so that samples with larger precipitates and high growth rates need less time to reach the peak hardness at the subsequent ageing of 150 °C. It has been reported that, pre-ageing is an effective way to form stabilized GP zones, which can act as precursors to form T' phase and η' phase, and then accelerate the ageing process [38]. During the first ageing at 120 °C, as discussed in Section 4.1, the phase fraction of η' phase increases with the decrease of that of T' phase. After ageing for 0.5 h at the first stage, numerous GP zones are formed with a few T' phase and η' phase. The formation of η' phase is easier at 120 °C than that at 150 °C, and its phase fraction increases with the increase of ageing time at 120 °C. Therefore, the phase fraction of η' phase of sample aged at 120 °C for 0.5 h should be higher than that aged at 150 °C for 0.5 h (17%) and lower than that aged at 120 °C for 12 h (25%). When the sample is further aged at 150 °C for 12 h at the second stage ($L_{0.5}H_{12}$), the precipitates consist of 78% T' phase and 22% η' phase. Therefore, it is reasonable to deduce that the phase fractions of T' phase and η' phase are almost unchanged during the second-stage ageing at 150 °C in the $L_{0.5}H_{12}$ sample. If the sample is aged for 12 h at the first stage, the precipitates consist of 75% T' phase and 25% η' phase, which also approximate the values after second-stage ageing at 150 °C for 2 h (74% T' phase and 26% η' phase, $L_{12}H_2$ sample), as shown in Fig. 9(b). It correlates well with the evolution of phase fraction during single-stage ageing reported in Section 4.1, i.e., the phase fractions of T' phase and η' phase do not change during the ageing process at 150 °C. In this case, there are still plenty of GP zones during the first-stage ageing, which can transform into T' phase and η' phase. Such phenomenon remains even if further extending the ageing time at the first stage from 12 to 24 h (Fig. 6(b)). Thus, the unchanged phase fraction of the $L_{12}H_2$ sample during the second-stage ageing at 150 °C is due to the dynamic balance of phase transformation from GP zones to T' and η' phases.

In contrast, the HL samples are aged at 150 °C first and followed by a second one at 120 °C. As listed in Table 1, when prolonging the first-stage ageing time from 0.5 to 8 h, the time to reach the peak hardness in the second ageing also increases from 8 to 20 h, contrary to that for LH samples. In this scenario, the formation and coarsening of precipitates are faster during the first-stage ageing at 150 °C than those at 120 °C (as indicated in Figs. 3(a) and (d)). This results from the higher precipitation driving force [39] and higher diffusion rate of solutes, which causes a fast depletion of solutes, and the concentration of solutes decreases with the increase of ageing time. Extending ageing time causes a lower concentration of solutes after

the first-stage ageing. The solubility of solutes decreases as the ageing temperature declines to 120 °C during the second-stage ageing. As a result, the Al matrix becomes supersaturated, which drives the secondary precipitation [40]. Meanwhile, the lower diffusion rate of solutes causes a slower growth rate of precipitates at 120 °C, as shown in Fig. 9(a). Therefore, a longer time at the first-stage ageing of 150 °C leads to a lower concentration of solutes in the matrix, which slows down the subsequent precipitation process. As for the HL samples, the phase fractions of precipitates almost remain constant during the first-stage ageing at 150 °C. The phase fraction of η' phases increases with the decrease of T' phases during the second stage-ageing (Fig. 9(b)), which is resulted from the occurrence of secondary precipitation. In addition, there are enough solutes remaining in the matrix after the first-stage ageing at 150 °C for a short time, therefore a higher phase fraction of η' phase remains in the $H_{0.5}L_8$ sample than that in the H_8L_{20} sample.

4.3 Contribution of T' phase and η' phase to strengthening

As shown in Fig. 10, the strain caused by η' phase is larger than that caused by T' phase in the matrix, in which larger lattice strain is the benefit from the improvement of the strength [41]. It is also verified by the higher peak hardness of the sample aged at 120 °C, which possesses a higher phase fraction of η' phase than that at 150 °C. That is to say, η' phase shows a better strengthening effect than T' phase as an individual phase. More complex factors of precipitates should be considered in the case of numerous precipitation, e.g., type, morphology, size, number density and volume fraction. Generally, the total precipitation strengthening of Al−Zn−Mg−Cu alloys (σ_p) can be well predicted by using the Kocks statistical model [3]:

$$\sigma_p = 0.6MGb\left\{2\sqrt{f_v}/[D_p/(\pi/4)]\right\} \quad (3)$$

where M(=2) is the Taylor factor, G(=26 GPa) is the shear modulus, b(=0.286 nm) is the magnitude of Bergers vector, f_v is the volume fraction of precipitates and D_p is the average diameter of precipitates. According to Eq. (3), the precipitation strengthening of T' phase and η' phase can be quantitatively calculated by obtaining the parameters of f_v and D_p for precipitates. However, Eq. (3) is only applied for spherical precipitates, so it is not suitable for η' phase with a plate-like morphology. A modified equivalent spherical model of η' phase has been developed, which has the same volume as the plate-like η' phase:

$$V_{\text{modified spherical model}} = V_{\text{plate-like }\eta'} \quad (4)$$

The equivalent diameter D_e of η' phase can be deduced from Eq. (4):

$$D_e = (6\bar{D}^2\bar{T})^{1/3} \quad (5)$$

where $\bar{D}$ is the average diameter of η' phase, and $\bar{T}$ is the average thickness of η' phase.

When there are different precipitates in alloy, the σ_p can be expressed as

$$\sigma_p = \sqrt{\sigma_{p_1}^2 + \sigma_{p_2}^2 + \cdots + \sigma_{p_n}^2} \quad (6)$$

where σ_{p_1}, σ_{p_2}, ⋯, σ_{p_n} are the strengthening contributions of precipitates.

Thus, the strengthening contributions of T' phase ($\sigma_{T'}$) and η' phase ($\sigma_{\eta'}$) and the total precipitation strengthening σ_p can be calculated by using Eqs. (3)−(6). The validity of this strengthening model has been verified in our previous work [24]. As a result, the predicted precipitation strengthening contributions of T' phase and η' phase are presented in Figs. 11(a) and (b). It is obvious that the predicted precipitation strengthening is influenced by the combination of the number density and diameter of precipitates. For both T' phase and η' phase, the diameter of precipitates has few contribution to the precipitation contribution when the number density is less than 0.5×10^{23} m^{-3}; however, when the number density is larger, increasing the diameter can make a much stronger contribution to the precipitation strengthening. The total precipitation strengthening from T' phase and η' phase is calculated and shown in Fig. 11(c), where both T' phase and η' phase can provide a great contribution to strengthening. These parameters for the prediction of precipitation strengthening used in Eqs. (3)−(6) can be easily obtained from TEM analysis. Therefore, the precipitation strengthening effect can be predicted with the characterization of the microstructures, which provides the possibility to understand the precipitates at the nanoscale and evaluate their strengthening contributions at the macroscale.

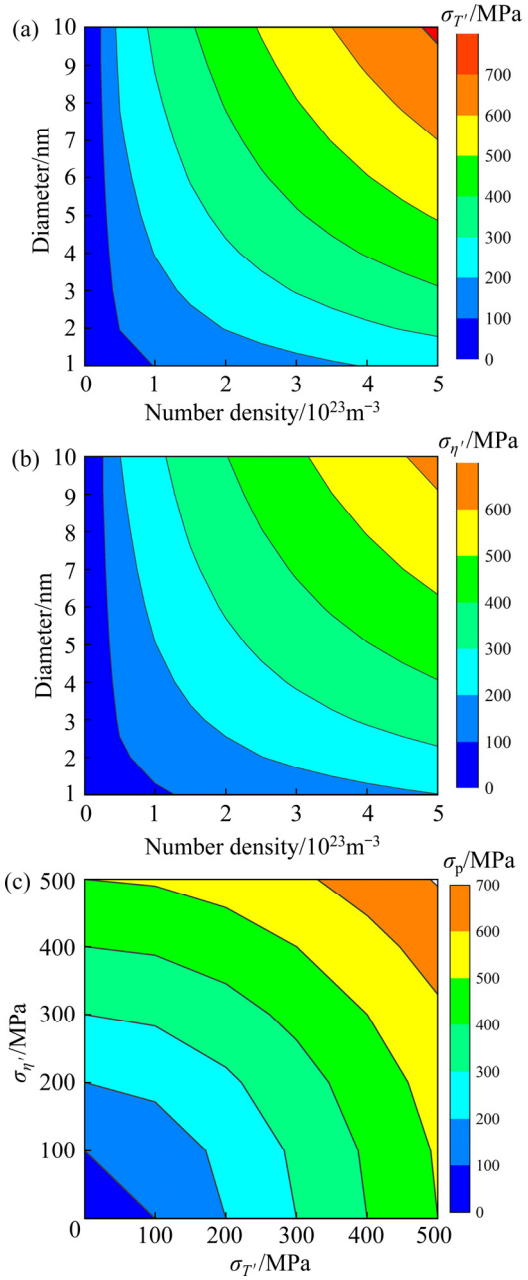

Fig. 11 Maps showing predicted precipitation strengthening contributions of T' phase (a) and η' phase (b) as function of number density and average diameter, and predicted precipitation strengthening as function of $\sigma_{T'}$ and $\sigma_{\eta'}$ (c)

5 Conclusions

(1) The precipitation of η' phase is promoted by the lower ageing temperature, so the Al−Zn−Mg−Cu alloy aged at 120 °C shows higher peak hardness than the alloy aged at 150 °C due to the higher number density of precipitates and phase fraction of η' phase.

(2) When sample is aged at 120 °C, the phase fraction of η' phase increases with the increase of ageing time, accompanied by the decrease of T' phase; whereas, the phase fractions of the two phases almost remain constant during the ageing process at 150 °C.

(3) Two-stage ageing with different ageing paths can successfully tailor the phase fractions of T' phase and η' phase, which can provide potential to improve the comprehensive performance of alloys while keeping their strength at the same level of T6.

(4) η' phase shows larger strains along the diameter direction (ε_{xx}=2.4%) than those along thickness direction (ε_{yy}=1.1%), while the strains introduced by T' phase are similar (ε_{xx}=1.2% and ε_{yy}=1.5%) in different directions.

(5) Precipitation strengthening contributions of T' phase and η' phase are evaluated using a modified strengthening model, which explains how precipitation strengthening is influenced by the combination of the number density and diameter of precipitates.

Acknowledgments

The authors are grateful for the financial supports from the National Natural Science Foundation of China (No. 51871033).

References

[1] AZARNIYA A, TAHERI A K, TAHERI K K. Recent advances in ageing of 7xxx series aluminum alloys: A physical metallurgy perspective [J]. Journal of Alloys and Compounds, 2019, 781: 945−983.

[2] PENG Ying-hao, LIU Chong-yu, WEI Li-li, JIANG Hong-jie, GE Zhen-jiang. Quench sensitivity and microstructures of high-Zn-content Al−Zn−Mg−Cu alloys with different Cu contents and Sc addition [J]. Transactions of Nonferrous Metals Society of China, 2021, 31: 24−35.

[3] GHIAASIAAN R, SHANKAR S. Structure−property models in Al−Zn−Mg−Cu alloys: A critical experimental assessment of shape castings [J]. Materials Science and Engineering A, 2018, 733: 235−245.

[4] ZHU A W, STARKE E A Jr. Strengthening effect of unshearable particles of finite size: A computer experimental study [J]. Acta Materialia, 1999, 47: 3263−3269.

[5] LIU Gang, SUN Jun, NAN Ce-wen, CHEN Kang-hua. Experiment and multiscale modeling of the coupled influence of constituents and precipitates on the ductile fracture of heat-treatable aluminum alloys [J]. Acta Materialia, 2005, 53: 3459−3468.

[6] STEMPER L, TUNES M A, DUMITRASCHKEWITZ P, MENDEZ-MARTIN F, TOSONE R, MARCHAND D, CURTIN W A, UGGOWITZER P J, POGATSCHER S. Giant

hardening response in AlMgZn(Cu) alloys [J]. Acta Materialia, 2021, 206: 116617.

[7] BENDO A, MATSUDA K, LEE S, NISHIMURA K, NUNOMURA N, TODA H, YAMAGUCHI M, TSURU T, HIRAYAMA K, SHIMIZU K, GAO H Y, EBIHARA K, ITAKURA M, YOSHIDA T, MURAKAMI S. Atomic scale HAADF-STEM study of η' and η_1 phases in peak-aged Al−Zn−Mg alloys [J]. Journal of Materials Science, 2018, 53: 4598−4611.

[8] BAKHSHI R, FARSHIDI M H, SAJJADI S A. Strengthening of aluminium alloy 7005 through imposition of severe plastic deformation supplemented by different ageing treatments [J]. Transactions of Nonferrous Metals Society of China, 2021, 31: 2909−2921.

[9] LÖFFLER H, KOVÁCS I, LENDVAI J. Decomposition processes in Al−Zn−Mg alloys [J]. Journal of Materials Science, 1983, 18: 2215−2240.

[10] HUANG Z W, LORETTO M H, SMALLMAN R E, WHITE J. The mechanism of nucleation and precipitation in 7075−0.7Li alloy [J]. Acta Metallurgica et Materialia, 1994, 42: 549−559.

[11] SHA G, CEREZO A. Early-stage precipitation in Al−Zn−Mg−Cu alloy (7050) [J]. Acta Materialia, 2004, 52: 4503−4516.

[12] ZOU Yan, CAO Ling-fei, WU Xiao-dong, WANG Yi-chang, SUN Xuan, SONG Hui, COUPER M J. Effect of ageing temperature on microstructure, mechanical property and corrosion behavior of aluminum alloy 7085 [J]. Journal of Alloys and Compounds, 2020, 823: 153792.

[13] LIU J, CHENG Y S, CHAN S W N, SUNG D. Microstructure and mechanical properties of 7075 aluminum alloy during complex thixoextrusion [J]. Transactions of Nonferrous Metals Society of China, 2020, 30: 3173−3182.

[14] TAKATA N, ISHIHARA M, SUZUKI A, KOBASHI M. Microstructure and strength of a novel heat-resistant aluminum alloy strengthened by T-$Al_6Mg_{11}Zn_{11}$ phase at elevated temperatures [J]. Materials Science and Engineering: A, 2019, 739: 62−70.

[15] LIU Ji-zi, HU Rong, ZHENG Jia-ling, ZHANG Yi-dong, DING Zhi-gang, LIU Wei, ZHU Yun-tian, SHA Gang. Formation of solute nanostructures in an Al−Zn−Mg alloy during long-term natural aging [J]. Journal of Alloys and Compounds, 2020, 821: 153572.

[16] STEMPER L, TUNES M A, OBERHAUSER P, UGGOWITZER P J, POGATSCHER S. Age-hardening response of AlMgZn alloys with Cu and Ag additions [J]. Acta Materialia, 2020, 195: 541−554.

[17] YANG X B, CHEN J H, LIU J Z, QIN F, XIE J, WU C L. A high-strength AlZnMg alloy hardened by the T-phase precipitates [J]. Journal of Alloys and Compounds, 2014, 610: 69−73.

[18] DAI Pan, LUO Xian, YANG Yan-qing, KOU Zong-de, HUANG Bin, WANG Chen, ZANG Jin-xin, RU Ji-gang. Nano-scale precipitate evolution and mechanical properties of 7085 aluminum alloy during thermal exposure [J]. Materials Science and Engineering A, 2018, 729: 411−422.

[19] FENG Chun, SHOU Wen-bin, LIU Hui-qun, YI Dan-qing, FENG Yao-rong. Microstructure and mechanical properties of high strength Al–Zn–Mg–Cu alloys used for oil drill pipes [J]. Transactions of Nonferrous Metals Society of China, 2015, 25: 3515−3522.

[20] ZHAO H, GAULT B, PONGE D, RAABE D. Reversion and re-aging of a peak aged Al−Zn−Mg−Cu alloy [J]. Scripta Materialia, 2020, 188: 269−273.

[21] WANG Yi-chang, WU Xiao-dong, CAO Ling-fei, TONG Xin, COUPER M J, LIU Qing. Effect of trace Er on the microstructure and properties of Al−Zn−Mg−Cu−Zr alloys during heat treatments [J]. Materials Science and Engineering A, 2020, 792: 139807.

[22] LIU Li, JIA Ying-ying, JIANG Jian-tang, ZHANG Bo, LI Guo-ai, SHAO Wen-zhu, ZHEN Liang. The effect of Cu and Sc on the localized corrosion resistance of Al−Zn−Mg−X alloys [J]. Journal of Alloys and Compounds, 2019, 799: 1−14.

[23] WANG Yi-chang, WU Xiao-dong, CAO Ling-fei, TONG Xin, ZOU Yan, ZHU Qian-qian, TANG Song-bai, SONG Hui, GUO Ming-xing. Effect of Ag on aging precipitation behavior and mechanical properties of aluminum alloy 7075 [J]. Materials Science and Engineering A, 2021, 804: 140515.

[24] ZOU Yan, WU Xiao-dong, TANG Song-bai, ZHU Qian-qian, SONG Hui, GUO Ming-xing, CAO Ling-fei. Investigation on microstructure and mechanical properties of Al−Zn−Mg−Cu alloys with various Zn/Mg ratios [J]. Journal of Materials Science & Technology, 2021, 85: 106−117.

[25] ZOU Yan, WU Xiao-dong, TANG Song-bai, WANG Yi-chang, ZHAO Kai, CAO Ling-fei. The effect of pre-ageing/stretching on the ageing-hardening behavior of Al–Zn–Mg–Cu alloys correlated with Zn/Mg ratio [J]. Materials Science and Engineering A, 2022, 830: 142331.

[26] HOU Xiao-hu, LI Ji-jun, LIU Fei, YAN Liang-ming, BAI Pu-cun. Coherent strain of Guinier–Preston II zone in an Al−Zn−Mg−Cu alloy [J]. Micron, 2019, 124: 102711.

[27] HOU Xiao-hu, BAI Pu-cun. Evaluation of strain fields caused by the η' phase in an Al−Zn−Mg−Cu alloy [J]. Materials Science and Engineering A, 2017, 683: 90−93.

[28] ZOU Yan, WU Xiao-dong, TANG Song-bai, ZHU Qian-qian, SONG Hui, CAO Ling-fei. Co-precipitation of T' and η' phase in Al−Zn−Mg−Cu alloys [J]. Materials Characterization, 2020, 169: 110610.

[29] KILAAS R. Optimal and near-optimal filters in high-resolution electron microscopy [J]. Journal of Microscopy, 1998, 190: 45−51.

[30] KHALFALLAH A, RAHO A A, AMZERT S, DJEMLI A. Precipitation kinetics of GP zones, metastable η' phase and equilibrium η phase in Al−5.46wt.%Zn−1.67wt.%Mg alloy [J]. Transactions of Nonferrous Metals Society of China, 2019, 29: 233−241.

[31] XIAO Hong-yu, LI Yu-gang, GENG Ji-wei, LI Hong-ping, WANG Ming-liang, CHEN Dong, LI Zhu-guo, WANG Hao-wei. Effects of nano-sized TiB_2 particles and Al_3Zr dispersoids on microstructure and mechanical properties of Al–Zn–Mg–Cu based materials [J]. Transactions of Nonferrous Metals Society of China, 2021, 31: 2189−2207.

[32] JIANG L, WEN H M, YANG H, HU T, TOPPING T, ZHANG D L, LAVERNIA E J, SCHOENUNG J M. Influence of length-scales on spatial distribution and interfacial characteristics of B_4C in a nanostructured Al matrix [J]. Acta Materialia, 2015, 89: 327−343.

[33] INOUE H, SATO T, KOJIMA Y, TAKAHASHI T. The temperature limit for GP zone formation in an Al−Zn−Mg

alloy [J]. Metallurgical and Materials Transactions A, 1981, 12: 1429−1434.

[34] TANG H P, WANG Q D, LUO C, LEI C, LIU T W, LI Z Y, JIANG H Y, DING W J, FANG J, ZHANG J W. Effects of aging treatment on the precipitation behaviors and mechanical properties of Al−5.0Mg−3.0Zn−1.0Cu cast alloys [J]. Journal of Alloys and Compounds, 2020, 842: 155707.

[35] HUANG Z W, LORETTO M H, WHITE J. Influence of lithium additions on precipitation and age hardening of 7075 alloy [J]. Materials Science and Technology, 1993, 9: 967−980.

[36] CAO Cheng, ZHANG Di, ZHUANG Lin-zhong, ZHANG Ji-shan. Improved age-hardening response and altered precipitation behavior of Al−5.2Mg−0.45Cu−2.0Zn (wt%) alloy with pre-aging treatment [J]. Journal of Alloys and Compounds, 2017, 691: 40−43.

[37] GUO M X, LI G J, ZHANG Y D, SHA G, ZHANG J S, ZHUANG L Z, LAVERNIA E J. Influence of Zn on the distribution and composition of heterogeneous solute-rich features in peak aged Al−Mg−Si−Cu alloys [J]. Scripta Materialia, 2019, 159: 5−8.

[38] LEE Y S, KOH D H, KIM H W, AHN Y S. Improved bake-hardening response of Al−Zn−Mg−Cu alloy through pre-aging treatment [J]. Scripta Materialia, 2018, 147: 45−49.

[39] DESCHAMPS A, BRECHET Y. Influence of predeformation and ageing of an Al−Zn−Mg alloy — II. Modeling of precipitation kinetics and yield stress [J]. Acta Materialia, 1998, 47: 293−305.

[40] JIANG J T, TANG Q J, YANG L, ZHANG K, YUAN S J, ZHEN L. Non-isothermal ageing of an Al−8Zn−2Mg−2Cu alloy for enhanced properties [J]. Journal of Materials Processing Technology, 2016, 227: 110−116.

[41] YANG Ming-jun, CHEN Hao-nan, OREKHOV A, LU Qiang, LAN Xin-yue, LI Kai, ZHANG Shu-yan, SONG Min, KONG Yi, SCHRYVERS D, DU Yong. Quantified contribution of β'' and β' precipitates to the strengthening of an aged Al−Mg−Si alloy [J]. Materials Science and Engineering A, 2020, 774: 138776.

时效处理调控双相强化 Al−Zn−Mg−Cu 中 *T*′相和 *η*′相相分数

邹 衍[1]，吴晓东[1]，唐松柏[1]，赵 凯[1]，曹玲飞[1,2]

1. 重庆大学 材料科学与工程学院 轻合金国际联合实验室(教育部)，重庆 400044；
2. 重庆大学 沈阳材料科学国家研究中心，重庆 400044

摘 要：采用硬度测试和透射电镜研究 *T*′相和 *η*′相强化 Al−Zn−Mg−Cu 合金中析出相相分数的调控策略。结果表明，在 120 和 150 ℃的单级和双级时效处理条件下，试样中出现不同相分数组合的 *T*′相和 *η*′相。在 120 ℃时，较低的时效温度有利于 *η*′相析出，随着时效时间的延长，*η*′相的相分数增加；而在 150 ℃时效过程中，*T*′相和 *η*′相的相分数几乎保持不变。此外，采用几何相位分析技术分析 *T*′相和 *η*′相产生的应变场，并结合析出相的尺寸、相分数和数量密度，定量预测 *T*′相和 *η*′相对析出强化的宏观贡献。

关键词：Al−Zn−Mg−Cu 合金；时效行为；显微组织；双相强化

(Edited by Wei-ping CHEN)